Chun Xu
Telemedicine and Advanced
Technology Research Center,
Department of Defense Biotechnology
High Performance Computing
Software Applications Institute,
U.S. Army Medical Research
and Materiel Command,
Fort Detrick, MD 21702-5012

Amy Silder
Department of Bioengineering,
Stanford University,
Stanford, CA 94305-6175

Ju Zhang
Auckland Bioengineering Institute,
University of Auckland,
Auckland 1010, New Zealand

Julie Hughes
U.S. Army Research Institute
of Environmental Medicine,
Natick, MA 01760-5007

Ginu Unnikrishnan
Telemedicine and Advanced
Technology Research Center,
Department of Defense Biotechnology
High Performance Computing
Software Applications Institute,
U.S. Army Medical Research
and Materiel Command,
Fort Detrick, MD 21702-5012

Jaques Reifman[1]
Telemedicine and Advanced
Technology Research Center,
Department of Defense Biotechnology
High Performance Computing
Software Applications Institute,
U.S. Army Medical Research
and Materiel Command,
MCMR-TT, 504 Scott Street,
Fort Detrick, MD 21702-5012
e-mail: jaques.reifman.civ@mail.mil

Vineet Rakesh
Telemedicine and Advanced
Technology Research Center,
Department of Defense Biotechnology
High Performance Computing
Software Applications Institute,
United States Army Medical Research
and Materiel Command,
Fort Detrick, MD 21702-5012

An Integrated Musculoskeletal-Finite-Element Model to Evaluate Effects of Load Carriage on the Tibia During Walking

Prior studies have assessed the effects of load carriage on the tibia. Here, we expand on these studies and investigate the effects of load carriage on joint reaction forces (JRFs) and the resulting spatiotemporal stress/strain distributions in the tibia. Using full-body motion and ground reaction forces from a female subject, we computed joint and muscle forces during walking for four load carriage conditions. We applied these forces as physiological loading conditions in a finite-element (FE) analysis to compute strain and stress. We derived material properties from computed tomography (CT) images of a sex-, age-, and body mass index-matched subject using a mesh morphing and mapping algorithm, and used them within the FE model. Compared to walking with no load, the knee JRFs were the most sensitive to load carriage, increasing by as much as 26.2% when carrying a 30% of body weight (BW) load (ankle: 16.4% and hip: 19.0%). Moreover, our model revealed disproportionate increases in internal JRFs with increases in load carriage, suggesting a coordinated adjustment in the musculature functions in the lower extremity. FE results reflected the complex effects of spatially varying material properties distribution and muscular engagement on tibial biomechanics during walking. We observed high stresses on the anterior crest and the medial surface of the tibia at pushoff, whereas high cumulative stress during one walking cycle was more prominent in the medioposterior aspect of the tibia. Our findings reinforce the need to include: (1) physiologically accurate loading conditions when modeling healthy subjects undergoing short-term exercise training and (2) the duration of stress exposure when evaluating stress-fracture injury risk. As a fundamental step toward understanding the instantaneous effect of external loading, our study presents a means to assess the relationship between load carriage and bone biomechanics. [DOI: 10.1115/1.4034216]

Keywords: stress fracture, tibial stress and strain, finite-element analysis, gait mechanics

Introduction

The prevalence of stress-fracture injuries, especially in the lower extremity (including tibia and knee), remains a leading health concern for the United States (U.S.) military Service Members [1]. Epidemiological studies have shown that women are at a higher risk for developing stress-fracture injuries than men (1.5–5.0 times higher) during basic combat training [2].

There are many suspected risk factors, with their independent and interacting effects on the injury mechanisms still unclear. A substantial body of literature attributes training-induced stress-fracture injuries to repetitive, internal mechanical loading arising from training regimens, including training intensity, volume, type, frequency, and rate of change in the regimen [3]. Load carriage, an inevitable part of military life during both training and operations, further amplifies injury risk by inducing aberrant changes in gait mechanics and external forces experienced by the body [4,5]. Although there are no documented mechanistic links between load carriage and internal forces, physicians often advise patients with joint injuries to avoid carrying heavy loads [6]. Furthermore, the current etiologic hypothesis of stress-fracture injuries is that mechanical loading environment (i.e., bone stress and strain) regulates osteocytes within the bone matrix, and bone adapts to the loading environment by altering its geometry and improving its structure [7]. Excessive internal forces elevate bone mechanical stress and strain, generating microscopic fatigue damage in the form of cellular and extracellular degeneration that may lead to stress fracture [8]. An accurate estimation of internal mechanical loading environment during exercises is therefore integral for understanding the relationship between exercise and skeletal health. Characterizing how gait mechanics, joint reaction forces (JRFs), and bone stress/strain distributions respond to load carriage can assist in the systematic evaluation and design of load carriage and may help reduce injury rates.

Past telemeterized knee-replacement studies revealed that knee contact forces can be as high as three times the body weight (BW) during normal walking [9,10], suggesting even greater internal forces during strenuous activities or with heavy load carriage. To date, only a few bone strain measurements have been performed in humans, and substantial variations exist in response to different locomotive activities, experimental conditions, and measuring sites [11]. The technical challenges and ethical restrictions associated with implanting strain gauges in these experiments make them impractical for use in large numbers of healthy subjects [12]. As an alternative, computational musculoskeletal analysis approaches have been shown to predict JRFs that are comparable to in vivo measurements [13–15]. Moreover, musculoskeletal analysis enables quantification of muscle and JRFs necessary to replicate the complex mechanical environment surrounding the bone, which can be used to define physiologically realistic loading conditions for performing finite-element analysis (FEA) to characterize the spatiotemporal strain and stress distributions in the bone [16].

FEA has been accepted as a useful tool in biomedical research. However, models capable of predicting stress/strain distributions during various activities are rare, due to the challenges in specifying both subject-specific and activity-dependent input data, such as motion pattern, skeletal alignment, muscle physiology, bone-segment geometry, and tissue properties. The last two factors determine the accuracy of the reconstructed geometrical model and the suitability of the adopted material property model, whereas the remaining factors contribute to the dynamic internal joint and muscle forces acting on the bone (i.e., the loading conditions of the FEA). With the rapid advancements in computational power and imaging modalities, geometrical reconstruction and mesh generation can now be subject-specific and automated [17]. Techniques such as quantitative computed tomography (QCT)-based FEA have gained popularity due to their ability to incorporate both bone morphology and bone mechanical material properties. However, existing QCT-based FEA of the lower extremities (such as the tibia and the knee) generally has, by and large, been limited to biomechanical changes due to age- or disease-related bone degeneration and often uses idealized or highly simplified loading conditions (i.e., it only includes a few muscle forces) [18]. In contrast, exercise-related activities, such as walking while carrying loads, induce dynamic (time-varying) muscular and joint forces on the tibia. Therefore, evaluation of the risks of stress fracture from these exercise-related activities should

include physiologically relevant loading conditions. Hence, the objectives of this work are to incorporate physiologically realistic loading of the tibia along with spatially varying material properties to quantify the biomechanical impact of load carriage. To this end, we developed an integrated musculoskeletal and dynamic stress-modeling framework capable of determining the kinetics, JRFs, and tibial strains/stresses during normal walking and when carrying loads. We investigated the following hypotheses: (1) changes in lower-extremity JRFs in response to load carriage depend on joint location and time point in the gait cycle, (2) high tibial stresses due to walking occur at multiple locations in the tibia during the pushoff phase, and (3) cumulative tibial stress (i.e., stress–time exposure) distribution during one gait cycle differs from tibial stress distributions at any time point of the walking cycle.

Materials and Methods

Musculoskeletal Analysis and Inverse Dynamics. We used the AnyBody Modeling System[TM] (AnyBody Technology, Aalborg, Denmark) to perform the musculoskeletal analysis (Fig. 1) [14]. Our model was driven by the data obtained from the motion-capture experiments described by Silder et al. [5] and approved by the Stanford University Institutional Review Board. Briefly, a healthy female subject (body mass, 66 kg; age, 27 yr; and height, 1.7 m) free of current and past injury walked on a force-sensing treadmill at her preferred speed (1.3 m/s) carrying no load (0%, baseline model) and with an additional load of 10%, 20%, or 30% of BW using an adjustable weight vest. To mimic the motion-capture experiments, where approximately equal weight was applied in the front and back, we defined an external force directly to the center-of-mass (CoM) to replicate the load. The measured ground reaction forces (GRFs) reflected the mechanical impact of load carriage. We attached a backpack to the musculoskeletal model for visualization, with the weight defined as zero to minimize the change in anterior–posterior CoM location. Output from the motion-capture experiments included kinematics (tracked marker trajectories), kinetics (GRFs), and electromyography (EMG). Due to the lack of subject-specific medical images and musculoskeletal parameters, we used available anthropometrical data (e.g., height, body mass, fat percentage, and sex) to scale a previously validated musculoskeletal geometry model. This generic model was based on medical imaging data and cadaver dissection, including bones, muscles, subcutaneous fat volumes, bony landmarks, ligaments, muscle-attachment sites, line-of-action of muscle actuators, bone wrapping surfaces, and joint geometries [19]. The implemented musculoskeletal geometry model consisted of seven rigid bodies in the lower extremity, including pelvis, thigh, shank, and foot, and 55 Hill-type muscles per leg [20]. We modeled the hip joints as spherical joints to enable flexion/extension, internal/external rotation, and abduction/adduction movement. We modeled the knee and ankle joints as revolute joints allowing flexion/extension rotation. We modeled the patella segment to be connected to the femur and the tibia by a revolute joint and a patellar tendon, respectively. This patellofemoral joint does not allow translation but allows for a small amount of rotation.

Bone-segment lengths are difficult to measure because of uncertainties about the distances between light-reflective markers and actual joint positions underneath the tissue. We determined joint positions and orientations by minimizing the errors between markers defined in the model and those tracked in the experiment in a least-squares manner [21]. Thereafter, we computed muscle activities and JRFs over one gait cycle using an inverse dynamics approach by minimizing the sum of cubed muscle activities, where the muscle activity was defined as the muscle force divided by the muscle strength [14]. We performed the whole-body musculoskeletal analysis for walking with no load (0%, baseline) and with an additional load of 10%, 20%, and 30% of BW.
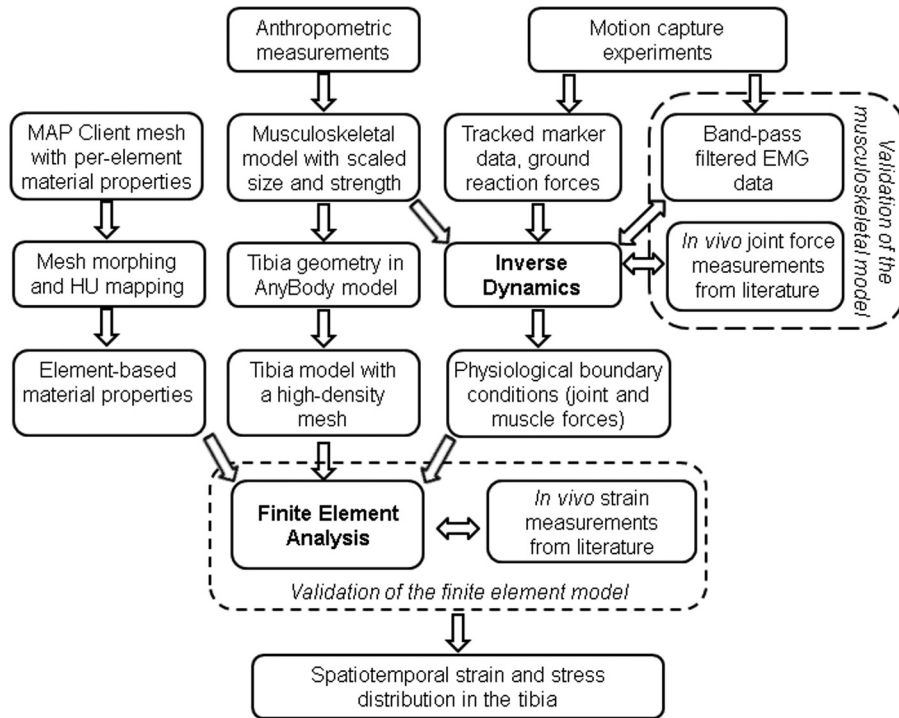
Fig. 1 Flowchart of the methodology. EMG: electromyography; HU: Hounsfield unit; and MAP: Musculoskeletal Atlas Project.

Finite-Element Analysis. Owing to the lack of subject-specific images for traditional geometrical reconstruction [22], we applied a host-mesh fitting (HMF) method [23] to morph the shape and map the spatially varying material properties from a source mesh onto the target mesh. To obtain the source mesh, we identified a sex-, age-, and body mass index (BMI)-matched subject from the Musculoskeletal Atlas Project (MAP) database [24], which contains data from the Victorian Institute of Forensic Medicine (Melbourne, VIC, Australia). We segmented the CT images of the MAP subject to create a high-quality (i.e., 2.0 mm average edge length) tetrahedral mesh (source mesh) with per-element Hounsfield units (HU) sampled from the images. We obtained the target mesh (i.e., the FEA model) by extracting the outer surfaces from the left tibia of the scaled musculoskeletal model as a stereolithography (STL) file. We refined and converted the STL mesh to a ten-node quadratic tetrahedral mesh using 3-matic v7 (Materialise, Leuven, Belgium). The tetrahedral elements in the target mesh possessed an average edge-length of 4.0 mm (determined using a mesh convergence study).

Next, we morphed the source mesh to the target mesh by minimizing the distance between the source and target mesh surfaces using a three-step mesh-morphing algorithm. Briefly, first we performed rigid registration and isotropic scaling to align the source mesh to the target mesh. Then, we embedded the source mesh into a host mesh [23] comprised of a single tricubic Lagrange element. Finally, we used the HMF method to morph the source mesh onto the geometry of the target mesh, which involved deforming the host mesh to minimize the least-squares distance between each node on the target mesh surface and its closest node on the source mesh surface. Internal nodes were excluded in the distance calculation because the two meshes had different resolutions, thus making it difficult to assign correspondence between internal nodes. Instead, internal nodes of the source mesh were passively deformed by the host mesh. We used Sobolev smoothing to ensure smooth host-mesh deformation and avoid element distortion [25].

After morphing the source mesh onto the geometry of the target mesh, we mapped the HU distribution of the deformed source mesh onto the target mesh by searching for the closest element. We assigned the median value of the nearest ten elements in the deformed source mesh to each target mesh element to achieve a smooth HU distribution and prevent artificial stress concentrations. We used the average distance between each node $\boldsymbol{p}$ on the target mesh surface and its closest node $\boldsymbol{q}$ on the morphed source mesh surface over the n nodes of the target mesh to evaluate the morphing error e

$$e = \left(\frac{1}{n} \sum_{i=1}^{n} \| \boldsymbol{p}_i - \boldsymbol{q}_i \|^2 \right)^{\frac{1}{2}}$$

To assure that no element distortion occurred as the result of mesh morphing, we examined the percentage of elements that failed the following quality criteria in the morphed source mesh: aspect ratio >5, skewness >60, Jacobian ratio <0.7, minimum angle <20 deg, and maximum angle >120 deg.

After mesh morphing, we converted the resultant HU values obtained in the target mesh into apparent densities and then to elastic modulus using a procedure similar to that used by Morgan et al. [26]. We assigned a Poisson's ratio of 0.325 and 0.167 for the bone region (HU > 100) and the intramedullary tissue region (HU < 100), respectively [27]. All the extracted material properties were modeled as linear elastic and isotropic. This procedure produced 135,897 unique material properties for the tibia model. Using an in-house-developed Tool Command Language script, we exported the material property definitions into an ABAQUS input file for structural analysis (ABAQUS 6.12, Dassault Systèmes, Vélizy-Villacoublay, France).

We exported muscle forces and bone forces/moments obtained from the whole-body musculoskeletal analysis in a local coordinate system defined at the tibial plateau as loading conditions in the FEA (Fig. A-1 in Supplemental Materials). The process included identifying positions of muscle and ligament attachment nodes in the FE mesh, exporting each force/moment component as concentrated loads, and defining coupling constraints between

---

Journal of Biomechanical Engineering

Table 1 Comparison of the model-predicted peak joint reaction forces (JRF) with published in vivo data

Source	Subject age (yr)	Hip JRF (BW)	Knee JRF (BW)
Present study	27	4.3	4.4
Bergmann et al. (1993)	69–82	4.1	N/A
Brand et al. (1994)	72	3.3	N/A
Bergmann et al. (2001)	51–76	2.9	N/A
Lu et al. (1997)	47–48	N/A	3.2
Taylor et al. (1998)	41	N/A	2.5
Taylor et al. (2001)	41–69	N/A	2.8
D'Lima et al. (2005)	80	N/A	2.8

BW: Body weight.

the created nodes and the tibial surface. We adopted radius values defined in AnyBody, ranging from 1 to 3 cm, for force application patches on all the muscles, and defined a total of 171 couplings between the tibial outer surface and the muscles/joints. Thereafter, we performed a sequence of 50-step, quasi-static loading simulations to obtain the tibial stress/strain distributions during one gait cycle.

To account for the cumulative effects of tibial stress, we calculated stress–time exposure (in MPa·s) over the tibial surface by integrating the FEA-predicted nodal contact stress values throughout the entire gait cycle. Thereafter, to quantify the change in volume engagement (i.e., volumetric fraction) of stress and stress–time exposure with load carriage, we first determined four pseudothresholds of stress from the baseline model that divided the cortical zone into five parts with equal volume. We conducted the same process in the baseline model to identify another four pseudothresholds of stress–time exposure distribution. Using these two series of pseudothresholds defined from the baseline model, we calculated the change in volume engagement due to loads of 10%, 20%, and 30% of BW. Finally, in the absence of any specified damage threshold above which the mechanical loading exerted on the tibia might be harmful, we defined ad hoc "high" stress and stress–time exposure to be the pseudothresholds that maximally discriminated the impacts of load carriage [28].

Results

Model Assessment

Musculoskeletal Analysis. Because invasive JRF measurements are impractical in healthy subjects, we compared our baseline no-loaded walking predictions with the available literature data of elderly patients who received total joint replacements (Table 1) [29–35] to ascertain that our model predictions were within the physiological limits. The experimentally measured peak JRF values ranged from 2.9 to 4.1 BW at the hip and 2.5 to 3.2 BW at the knee compared to our model predictions of 4.3 and 4.4 BW at the hip and knee, respectively. Moreover, we compared the predicted muscle activations necessary to produce the measured dynamic marker trajectories during experiments with EMG measurements (Fig. 2) [36]. The predicted and measured muscle activities show similar features, including biphasic activation of the dorsiflexor (e.g., tibialis anterior, see Fig. 2(a)); activation of quadriceps during early stage of the stance (e.g., vastus lateralis, vastus medialis, and rectus femoris, see Figs. 2(b)–2(d)); and activation of plantarflexors before pushoff (e.g., gastrocnemius and soleus, see Figs. 2(e) and 2(f)).

Finite-Element Analysis. We compared the in vivo tibial strain measured at the medial side of the midtibia [37], which was the only available tibial strain profile during one walking cycle in an age-matched subject, to the predicted axial-strain profiles from the baseline model at the corresponding cross-sectional plane. After adjusting for body weight and stride length, the predicted axial-strain profiles obtained at the medial line of the midshaft of the tibia showed two pronounced peaks (Fig. 3), consistent with the in vivo data [37]. At the first, and lower, of the two peaks, the simulations underestimated the strains in the anterior border (i.e., the anterior crest) (Fig. 3(a)) and considerably overestimated them in the posterior aspect of the tibia (Fig. 3(b)). The second, and higher, peak, occurred in the late stance phase and showed good agreement with the in vivo data [37]. The predicted peak tibial principal strains ([371.6 (standard deviation (SD) = 92.7) $\mu\varepsilon$] for tension and -716.1 (SD = 203.7) $\mu\varepsilon$ for compression) were within the range of in vivo strain measurements during walking reported in the literature (i.e., 237–1250 $\mu\varepsilon$) [38].
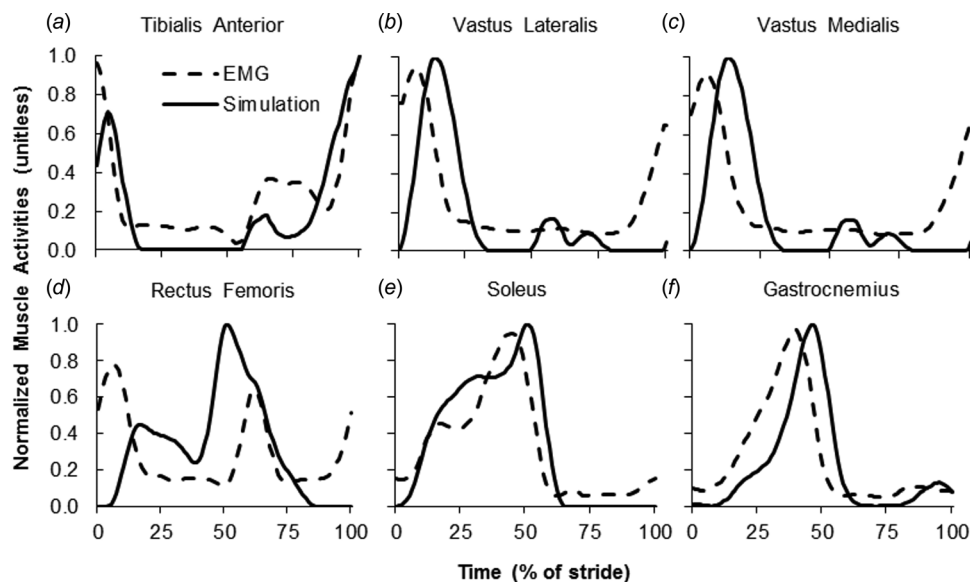

Fig. 2 Comparison of muscle activities predicted by the model (solid lines) and measured by electromyography (EMG, dashed lines) as a function of percent of stride. We normalized magnitudes to the maximum values for each curve.
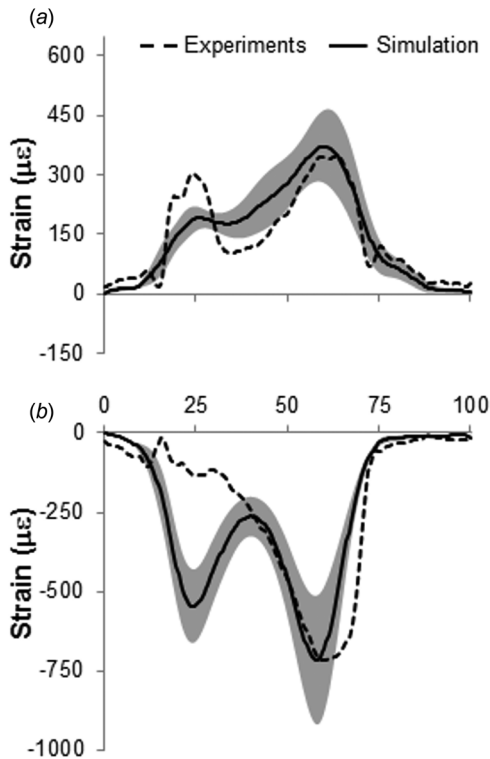
(a)

(b)

Fig. 3 Comparison of the in vivo tibial strain measurements (dashed lines) and model predictions at the medial side of the midshaft. Solid lines denote the simulated axial-strain curves averaged over the (a) anterior and (b) posterior aspects of the tibia, with the shaded region representing one standard deviation.

Mesh Morphing. Visual examination revealed that the morphed source tibia (Fig. 4(a), blue) possessed very similar shape and geometry as the target tibia (Fig. 4(a), red). Quantitatively, the error e between the morphed source mesh and the target mesh was 5.9 mm after rigid registration, which was reduced to 1.4 mm after HMF. The largest discrepancy occurred in the distal end, due to the complexity of the structure and, specifically, the presence of the medial malleolus. The percentage of elements that failed the mesh quality assessment was less than 0.8%, indicating that the morphing algorithm was successful in reproducing the

shape of the target tibia and maintaining the mesh quality (i.e., without introducing element distortion). Figures 4(b)–4(e) showed the distribution of the tibial Young's modulus in different views, suggesting that the Young's modulus was higher on the medial surface and lower on the lateral surface. Furthermore, a coronal cross section revealed higher Young's moduli in the cortical region of the diaphysis (Fig. 4(f)).

Kinetics and Kinematics. Figure 5 shows the temporal evolution of muscle activities when walking with 30% of BW during one gait cycle. Changes in joint kinematics in response to load carriage (Figs. 6(a)–6(f)) were in good agreement with the prior work [5]. In the baseline model, the ankle was exposed to the highest internal forces (4.7 BW), as compared with 4.4 BW and 4.3 BW at the knee and hip, respectively. With additional 10%, 20%, and 30% of BW load, the JRFs increased, respectively, by 4.3%, 15.1%, and 16.4% at the ankle; 8.0%, 23.3%, and 26.2% at the knee; and 13.5%, 17.1%, and 19.0% at the hip (Figs. 6(g)–6(i); see Table S1, which is available under the "Supplemental Materials" tab for this paper on the ASME Digital Collection, for the changed joint kinematics and kinetics as a function of load carriage).

Tibial Stress and Strain. The spatiotemporal distribution of von Mises stresses suggested a relationship between elevated stress magnitudes and load carriage (Fig. 7). For all the cases of load carriage, von Mises stresses in the medial side of the diaphysis were higher than the remaining surfaces, with their locations expanding from the medial to the entire posterior aspect as the gait progressed. For the same time point, the peak stress region occurred at the proximal diaphysis, corresponding to the location of the semitendinosus muscle of the hamstring muscles. Compared to carrying no load, carrying an additional 30% of BW increased the magnitudes of peak von Mises stresses at pushoff from 24.1 MPa to 32.9 MPa at the anterior crest, and from 40.3 MPa to 58.5 MPa in the medial aspect of the tibia (Table 2).

The directions of principal stresses and strains were in alignment with the axial direction of the tibia. For all the load-carriage conditions, the anterior crest was exposed to tension, while the posterior aspect experienced compression. At pushoff, we observed the peak maximum principal strain (i.e., peak tensile strain) on the anterior crest, and the peak minimum principal strain (i.e., peak compressive strain) on the posterior surface and around the medial border. An extra 30% of BW load carriage increased the peak principal stress by 34.5% in the anterior crest and by 39.1% in the posterior aspect of the tibia compared to
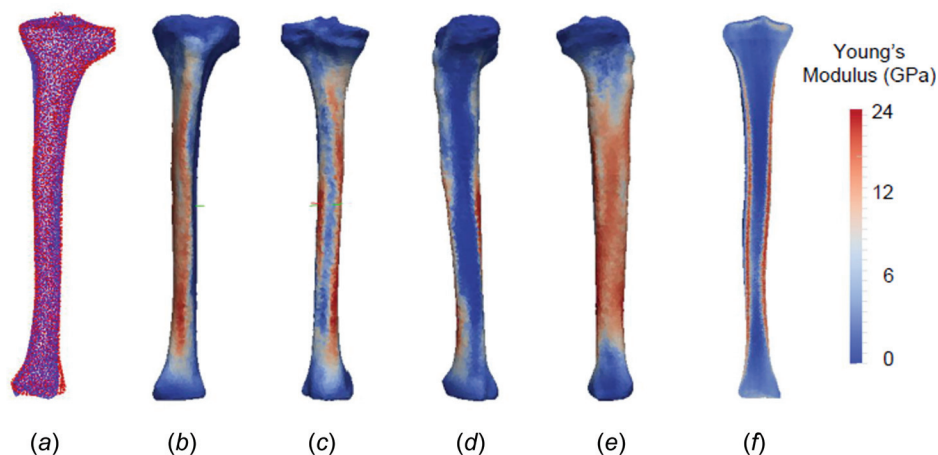

(a)   (b)   (c)   (d)   (e)   (f)

Fig. 4 Results from mesh morphing (a) and material mapping (b)–(f). In (a), the nodes of the deformed source mesh (blue) were overlaid onto the nodes of the target mesh (red). Mapped material properties superimposed on the tibial model are shown at anterior (b), posterior (c), lateral (d), medial (e), and a coronal cross section (f).
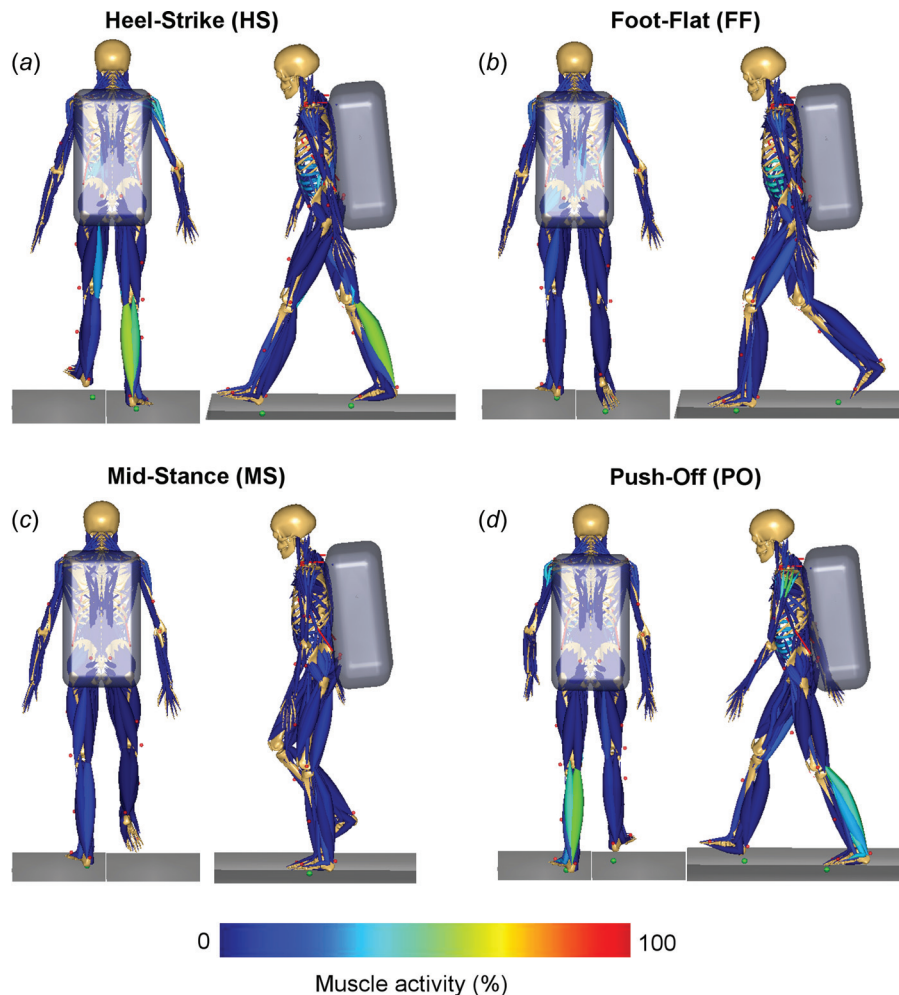
Fig. 5 Temporal evolution of muscle activities with 30% of body weight (BW) load carriage at heel-strike (HS, (*a*)), foot-flat (FF, (*b*)), midstance (MS, (*c*)), and pushoff (PO, (*d*)). At each time point, both anterior–posterior (left) and medial–lateral (right) views are shown. Muscle activity is described as 0–100% of maximum activity. At HS, the tibialis anterior is activated until the foot is completely in contact with the floor. Gluteus medius is activated before HS to prepare for load bearing and continues to be active throughout the first half of the stance phase. At FF, the hip moves slowly into extension caused by a contraction of muscles, such as the gluteus maximus. Extension of the knee is caused by a contraction of the quadriceps, and flexion is caused by a contraction of the hamstrings. At MS, the hip moves from flexion to extension by the contraction of the gluteus medius muscle. During PO, gastrocnemius and soleus are activated to accelerate the body forward, reaching more than 60% of muscle strength.

those of the baseline model. Peak stress and strain in the anterior crest (dashed lines) were 19.2 (SD = 3.9) MPa (Fig. 8(*a*)) and 1049.3 (SD = 108.6) $\mu\varepsilon$ (Fig. 8(*c*)), respectively, for baseline, and 23.5 (SD = 6.5) MPa (Fig. 8(*b*)) and 1223.9 (SD = 288.3) $\mu\varepsilon$ (Fig. 8(*d*)), respectively, for the 30% of BW load condition. Peak stress and strain in the posterior aspect (solid lines) were −35.3 (SD = 8.1) MPa (Fig. 8(*a*)) and −2497.3 (SD = 425.9) $\mu\varepsilon$ (Fig. 8(*c*)), respectively, for the baseline model, and −38.1 (SD = 15.7) MPa (Fig. 8(*b*)) and −3051.3 (SD = 761.7) $\mu\varepsilon$ (Fig. 8(*d*)), respectively, for the 30% load-carriage condition.

In the baseline model, we first identified four pseudothresholds in von Mises stress distribution at pushoff (5.3, 6.2, 8.6, and 14.5 MPa, see Fig. 9(*a*)), and four pseudothresholds in the stress–time exposure distribution (0.1, 0.3, 0.8, and 1.9 MPa·s, see Fig. 9(*b*)). The histograms of volume engagement of stress (Fig. 9(*a*)) and stress–time exposure (Fig. 9(*b*)) indicated that there was greater tibia volume subjected to higher stress and stress–time exposure with increasing loads. Additionally, the

percent of the tibia experiencing high stress (>14.5 MPa) increased from 20.0% in the baseline walking condition to 21.7%, 24.5%, and 25.1% when carrying 10%, 20%, and 30% of BW, respectively. The tibial volume experiencing high stress–time exposure levels (>1.9 MPa s) increased from 20.0% in the baseline walking condition to 21.1%, 23.4%, and 25.6% when the subject carried loads of 10%, 20%, and 30% of BW, respectively. Finally, considering the time of exposure to mechanical stress, the region subjected to "high mechanical loading" shifted from the anterior crest and the medial surface of the tibia to the medioposterior aspect of the tibia (Figs. 9(*c*) and 9(*d*)).

Discussion

To the best of our knowledge, this is the first study that integrated musculoskeletal and FE modeling approaches to determine the effects of load carriage on gait mechanics, JRFs, and tibial spatiotemporal stress/strain distributions. Compared with
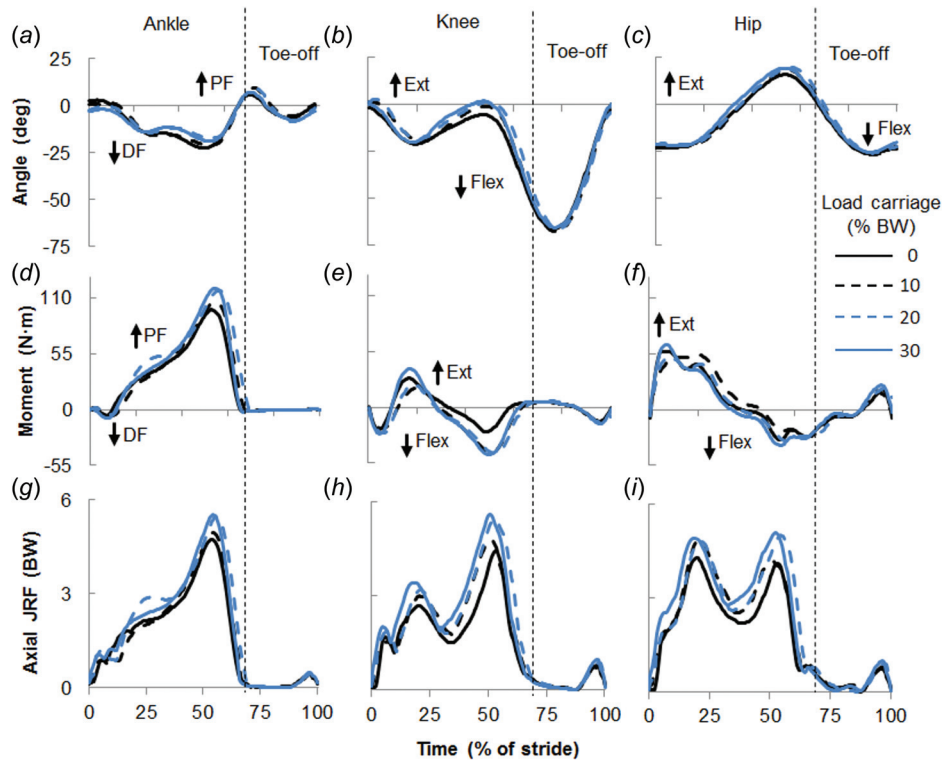
Fig. 6 Joint kinematics and kinetics for different loads during one gait cycle. Positive angles and moments represent extension, and negative values represent flexion. Forces are shown as normalized dimensionless quantities. BW: body weight; deg: degree; DF: dorsiflexion; Ext: extension; Flex: flexion; JRF: joint reaction force; and PF: plantar flexion.
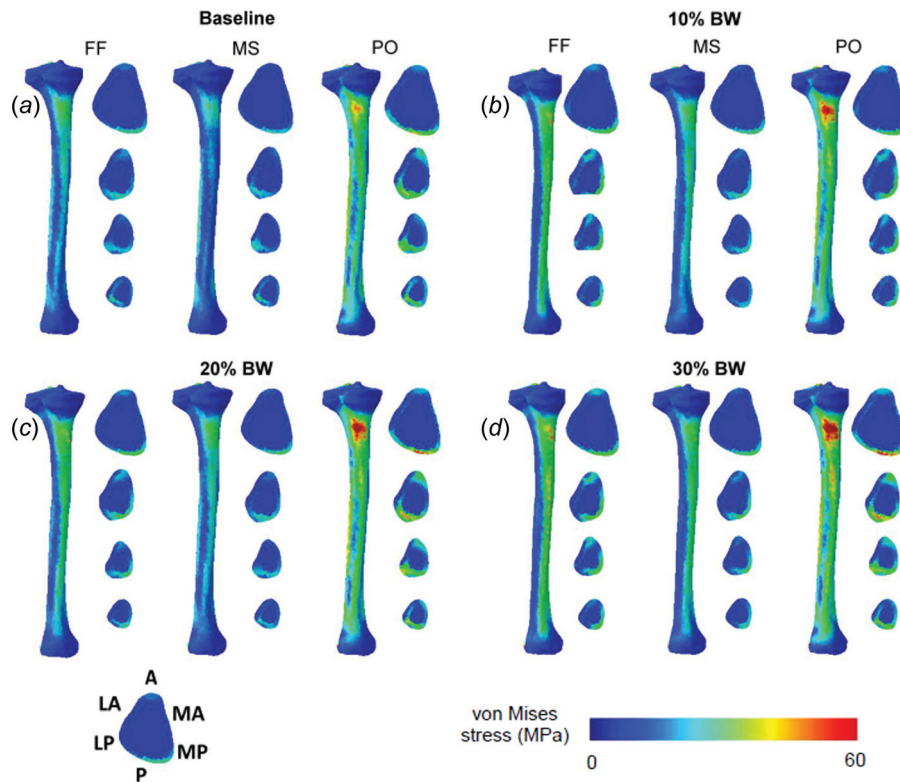

Fig. 7 Spatiotemporal distribution of tibial stresses during one gait cycle without (*a*) and with 10% (*b*), 20% (*c*), and 30% (*d*) body weight (BW) load carriage at foot-flat (FF), midstance (MS), and pushoff (PO). We divided the cross section of the left tibia into six sectors. A: anterior; MA: medial anterior; MP: medial posterior; P: posterior; LP: lateral posterior; and LA: lateral anterior.

Table 2 Model-predicted peak tibial von Mises stress at push-off for walking with no load (0%) and an additional 10%, 20%, and 30% of body weight (BW)

Load carriage (% BW)	Tension (MPa)	Compression (MPa)
0	24.1	40.3
10	28.7	48.5
20	32.3	57.6
30	32.9	58.5

commonly adopted, simplified loading conditions (i.e., with no, or only a few, muscle forces included), the incorporated muscle forces produced arguably more realistic deformations and strain distributions in the tibia. In support of our first hypothesis, we found that the change in JRFs in response to load carriage depends on joint location and time point in the gait cycle. In addition, the results suggest that load carriage increased JRFs at a rate disproportionate to that of the load carriage. Under all the load-carriage conditions, the greatest internal JRF occurred at the knee during the pushoff phase. In support of our second and third hypotheses, we observed greater stress on the anterior crest (tension) and the medial surface (compression) of the tibia at pushoff. Greater stress–time exposure occurred in the medioposterior aspect of the tibia. Our methods present a means to assess the relationship between load carriage and bone biomechanics for systematic evaluation and design of load carriage.

There are a few interesting observations from the FEA results. First, it is not surprising that load carriage increased both peak stress and bone volume experiencing high stresses (Figs. 7–9). However, the results provided insights on the locations of high-stress zones (i.e., the anterior crest and the medial aspect of the tibia) and that of high stress–time exposure (i.e., the medioposterior surface). Moreover, the stress distribution revealed the independent and interacting effects of spatially varying material property distribution and muscular engagement on tibial biomechanics during walking. Specifically, we observed two high-stress regions, coinciding with the area of higher elastic moduli (i.e., the anterior crest and the medial aspect of the tibia). Between these two regions, the one on the medial surface of the tibia corresponded to the location where the semitendinosus muscle inserted, while the one on the anterior crest of the tibia is close to the front muscles, such as the tibialis anterior. The engagement of the gastrocnemius, soleus, and the tibialis posterior muscles contributed to the increased high stress–time exposure in the medioposterior region of the tibia. Among the abovementioned muscle groups, the semitendinosus muscle is part of the hamstring muscle group, functioning as a major knee flexor and thigh extensor. It also helps to medially rotate the tibia on the femur when the knee is flexed and medially rotate the femur when the hip is extended. The tibialis anterior stabilizes the foot during the stance phase. The gastrocnemius is a powerful plantarflexor of the foot, which aids in pushing the body forward when a person walks or runs. The soleus and the tibialis posterior muscles are responsible for lifting the heel to support the subject's weight on the ball portion of the foot. Previous studies have shown that aberrant changes to these muscular activities can predispose the tibia to stress-fracture injury. For example, excessive training on hard surfaces may damage the tibialis anterior and may cause anterior tibial stress fracture [39], while excessive pronation (i.e., flat feet) and poor ankle biomechanics may fatigue the soleus and the tibialis posterior muscles, eventually causing posterior tibial stress fracture [40]. Through our musculoskeletal model, we were able to characterize the combined effect of the muscular engagement and the spatially varying material properties on the
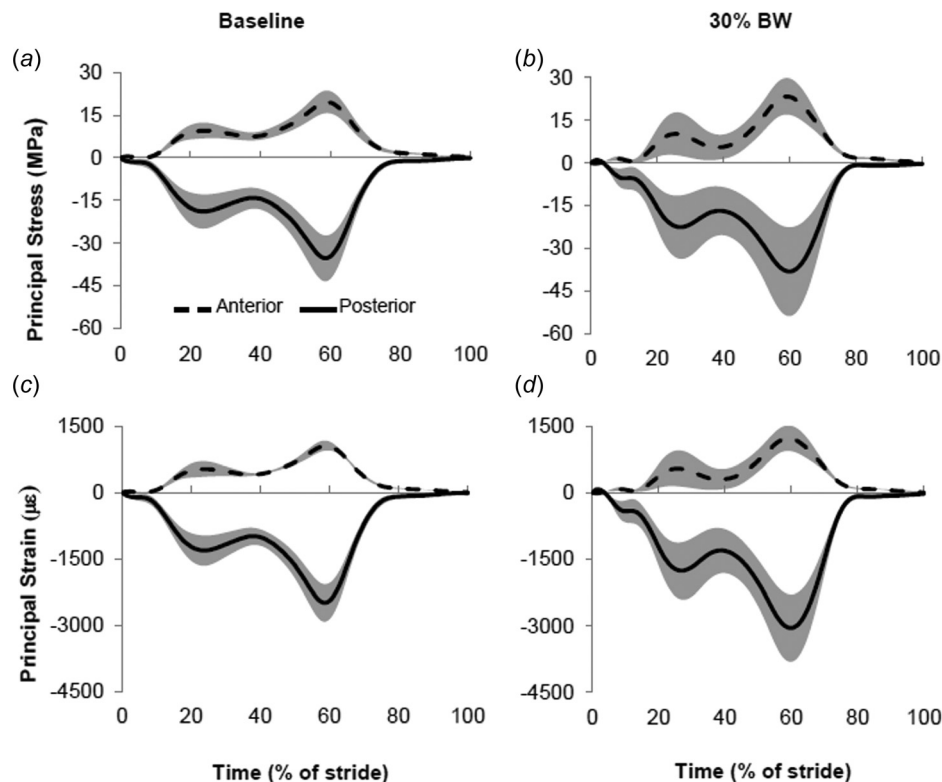

Fig. 8 Temporal evolution of principal stresses ((a) and (b)) and principal strains ((c) and (d)) averaged over the anterior crest (dashed lines) and the posterior aspects (solid lines) of the tibia for baseline (no load carriage) and 30% body weight (BW) load carriage conditions. Shaded region represents one standard deviation.
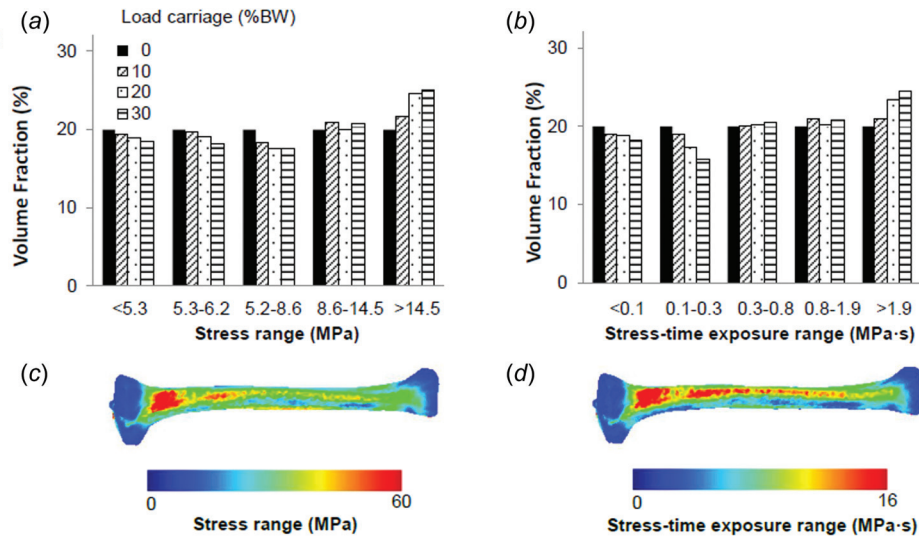
Fig. 9 Volume engagement histogram of (*a*) stress and (*b*) stress–time exposure under different load-carriage conditions. (*c*) Peak stress distribution at pushoff phase. (*d*) Cumulative stress–time exposure distribution over one gait cycle. BW: body weight.

biomechanical response of the tibia to load carriage, which may predispose the tibia to stress-fracture injury.

Second, our model predicted peak strain on the medioposterior aspect of the upper tibia (Figs. 6, 7, and 9), whereas experiments typically measure bone strains on the medial or anteromedial aspect, due to challenges associated with attaching strain staples or strain gauges underneath calf muscles [11]. This suggests that in vivo measurements are potentially underestimating the actual peak tibial strain. Finally, the percentage increase in peak compressive strain was greater than the peak tensile strain (39.1% versus 34.5%) when walking with 30% BW load carriage. This indicates different mechanisms by which the anterior and posterior portions of the diaphysis are subjected to injury susceptibility [41].

Prior studies suggest that both joint mechanical work and metabolic energy expenditure increase approximately linearly with carried load [42]. While all the lower-extremity joints contribute to the increased mechanical work, the patterns of the changes or the impacts on tibial stress/strain distributions are unclear. Our musculoskeletal analysis results suggested that the increases in JRFs due to load carriage were dependent on the phase of the gait cycle, as well as the location of the joint. Under all the load-carriage conditions, the highest JRFs occurred at the pushoff phase. This is because at this time point, the lever arm of the GRF caused an ankle plantar flexion moment and large activations of the soleus and gastrocnemius (Fig. 2). These muscle contractions, combined with the GRF, led to the highest internal loads at the ankle during a gait cycle. It was not entirely unexpected that internal JRFs at all the joints increased with load carriage (Fig. 6). However, the changes in JRFs were not proportional to load carriage (Table S1 is available under the "Supplemental Materials" tab for this paper on the ASME Digital Collection"), suggesting nonlinear and nonuniform changes in muscle activity due to load carriage [5]. This is likely a consequence of coordinated adjustments in the musculature to maintain balance and attenuate the effects of increased loads while walking. Our observations were consistent with previous reports regarding the paradoxical roles that muscles play in both injury development and prevention. Lower-extremity muscles exert more than 3–10 BW of compressive axial forces during everyday activity, such as walking [43], or during strenuous activity, such as running [44]. However, muscles also act to mitigate the load exerted on bone by dissipating forces as well as absorbing bending moments [45]. More importantly, results show that the knee JRF was most sensitive to

load carriage (26.2% increase at 30% of BW, compared with 16.4% at the ankle and 19.0% at the hip). Our results highlight the need to reduce aberrant knee JRFs to prevent knee injury, which is the most frequently observed noncombat musculoskeletal injury in the U.S. Army [4] and the civilian population, as well [46].

Bone strength is known to be heavily influenced by dynamic mechanical loading via adaptive bone formation that changes both its geometry and strength [7,47]. However, in the case of greater-than-customary loading (i.e., magnitude and/or frequency), stresses and strains that lead to functional adaptation of bone also lead to fatigue damage of bone and, potentially, stress fracture. Therefore, the characterization of internal mechanical loads, such as JRFs and stress/strain distributions in the bone, provides a more comprehensive assessment of bone biomechanics and an improved understanding of potential risk factors. Toward this end, our modeling framework provides a means to mechanistically study the dose–response relationships between whole-bone biomechanics and load carriage. The model can also be extended to study intersubject variability by incorporating high-resolution imaging and EMG data from healthy subjects under various exercise conditions. Furthermore, by using devices such as an accelerometer, it may be possible to use our model to correlate stress-fracture injury occurrence with individual training histories, and gain insights that could potentially be used to quantify bone damage thresholds and training capacity based on cumulative stress–time exposure.

Our model is limited by the assumptions employed to construct the model, and our inability to perform direct validation. From a practical standpoint, direct validation of the model predictions in healthy humans is not feasible. In an attempt to provide an element of validation of the developed methodology, we compared our model results with the literature and found the results to be within the physiological range (Fig. 3, Table 1, and Table S1 is available under the "Supplemental Materials" tab for this paper on the ASME Digital Collection). Moreover, by comparing the onset and offset timing of muscle activity, the predicted muscle-force profiles demonstrated good agreement with EMG measurements of muscle activation once electromechanical delays (estimated to be around 10% of gait cycle) were taken into account (Fig. 2). The "good" agreement referred to the similarity in the timing between the experimental and simulation results. Capturing these features of muscle activities was important because these muscles are the primary decelerators and accelerators of the body and therefore the

dominant factor contributing to the tibial stress/strain distributions (i.e., the loading forces).

Our musculoskeletal model predicted greater JRFs than experimentally observed (Table 1), and muscle activation lagged the EMG signal (Fig. 3). While musculoskeletal analysis based on maximizing muscle endurance and postponing fatigue has been extensively used, it has been reported to overpredict JRFs, compared to in vivo measurements [48]. However, experimental techniques, such as telemeterized axial force measurement that are based on the deformation of the fixation device, may frequently underestimate internal loads, as the implant site could carry some of the load, leading to reduced deformations in the device [49]. Furthermore, the available experimental JRFs used for comparisons were from older patients with joint replacements, and it is reasonable to expect reduced internal forces due to reduced muscle functions. Finally, an inherent electromechanical delay exists between the onset of electrical activity and measurable tension (muscle forces) [50], and a perfect correlation between EMG signal and estimated muscle forces would theoretically exist only if an EMG-driven objective function was to be incorporated. Another limitation of our musculoskeletal model stems from simplifying the knee joints as revolute joints. While it is adequate to describe the hip joints as standard ball–socket joints and the ankle–subtalar joints as revolute joints, the knee joint's motion is much more complex, including both translation and rotation. Previous studies have shown that skeletal misalignment increases the knee frontal plane moments during the stance, which may increase the risk of stress-fracture injury [51].

In the absence of subject-specific medical images, we were not able to reconstruct individualized tibial geometrical structure for the FEA. We scaled a 50th percentile European female generic musculoskeletal model using anthropometric measurements. Thereafter, we conducted a motion and parameter optimization procedure that not only constrained the model to follow the recorded marker trajectories but also optimized the subject's parameters, including segment lengths and marker placements. Statistical shape analysis of clavicular cortical bone using CT scans of 20 subjects revealed that bone length is responsible for the most significant anatomical variation in bone morphology, indicating that our model captured the primary morphological feature, despite some loss of regional details [52]. Similarly, we used tibial material properties mapped from a sex-, age-, and BMI matched subject for the FEA. This approach along with the use of linear elastic and isotropic material property assumption can affect the tibial stress/strain predictions. However, we expect that similar patterns of increased tibial stress/strain as the result of load carriage would be seen, had the subject-specific, anisotropic material property been applied. Individual musculoskeletal properties and bone morphology, which will undoubtedly improve the accuracy of injury risk, should be considered in future analysis. Nevertheless, we believe that the results from this study, along with the novel methodology to couple musculoskeletal analysis with FEA, represent a way forward to better understand internal loading in the bone and would benefit the orthopedic research community.

Acknowledgment

References

[1] Jones, B. H., and Hansen, B. C., 2000, "An Armed Forces Epidemiological Board Evaluation of Injuries in the Military," Am. J. Prev. Med., 18(Suppl. 3), pp. 14–25.

[2] Shaffer, R. A., Rauh, M. J., Brodine, S. K., Trone, D. W., and Macera, C. A., 2006, "Predictors of Stress Fracture Susceptibility in Young Female Recruits," Am. J. Sports Med., 34(1), pp. 108–115.

[3] Jones, B. H., Perrotta, D. M., Canham-Chervak, M. L., Nee, M. A., and Brundage, J. F., 2000, "Injuries in the Military: A Review and Commentary Focused on Prevention," Am. J. Prev. Med., 18(Suppl. 3), pp. 71–84.

[4] Seay, J. F., Fellin, R. E., Sauer, S. G., Frykman, P. N., and Bensel, C. K., 2014, "Lower Extremity Biomechanical Changes Associated With Symmetrical Torso Loading During Simulated Marching," Mil. Med., 179(1), pp. 85–91.

[5] Silder, A., Delp, S. L., and Besier, T., 2013, "Men and Women Adopt Similar Walking Mechanics and Muscle Activation Patterns During Load Carriage," J. Biomech., 46(14), pp. 2522–2528.

[6] Neumann, D. A., and Hase, A. D., 1994, "An Electromyographic Analysis of the Hip Abductors During Load Carriage: Implications for Hip Joint Protection," J. Orthop. Sports Phys. Ther., 19(5), pp. 296–304.

[7] Burr, D. B., 2011, "Why Bones Bend But Don't Break," J. Musculoskelet. Neuronal. Interact, 11(4), pp. 270–285.

[8] Martin, R. B., and Burr, D. B., 1982, "A Hypothetical Mechanism for the Stimulation of Osteonal Remodelling by Fatigue Damage," J. Biomech., 15(3), pp. 137–139.

[9] Kutzner, I., Heinlein, B., Graichen, F., Bender, A., Rohlmann, A., Halder, A., Beier, A., and Bergmann, G., 2010, "Loading of the Knee Joint During Activities of Daily Living Measured In Vivo in Five Subjects," J. Biomech., 43(11), pp. 2164–2173.

[10] Morrison, J. B., 1969, "Function of the Knee Joint in Various Activities," Biomed. Eng., 4(12), pp. 573–580.

[11] Yang, P. F., Bruggemann, G. P., and Rittweger, J., 2011, "What Do We Currently Know From In Vivo Bone Strain Measurements in Humans?" J. Musculoskelet. Neuronal. Interact, 11(1), pp. 8–20.

[12] Milgrom, C., Finestone, A., Simkin, A., Ekenman, I., Mendelson, S., Millgram, M., Nyska, M., Larsson, E., and Burr, D., 2000, "In-Vivo Strain Measurements to Evaluate the Strengthening Potential of Exercises on the Tibial Bone," J. Bone Jt. Surg. Br., 82(4), pp. 591–594.

[13] Kinney, A. L., Besier, T. F., D'Lima, D. D., and Fregly, B. J., 2013, "Update on Grand Challenge Competition to Predict In Vivo Knee Loads," ASME J. Biomech. Eng., 135(2), p. 021012.

[14] Damsgaard, M., Rasmussen, J., Christensen, S. T., Surma, E., and Zee, M., 2006, "Analysis of Musculoskeletal Systems in the AnyBody Modeling System," Simul. Modell. Pract. Theory, 14(8), pp. 1100–1111.

[15] Manders, C., New, A., and Rasmussen., J., 2008, "Validation of Musculoskeletal Gait Simulation for Use in Investigation of Total Hip Replacement," J. Biomech., 41(S1), p. S488.

[16] Gaofeng, W., Xueling, B., Hongsheng, W., Zengliang, F., and Chengtao, W., 2009, "Component Mode Synthesis Approach to Estimate Tibial Strains in Gait," J. Med. Eng. Technol., 33(6), pp. 488–495.

[17] Poelert, S., Valstar, E., Weinans, H., and Zadpoor, A. A., 2013, "Patient-Specific Finite Element Modeling of Bones," Proc. Inst. Mech. Eng., Part H, 227(4), pp. 464–478.

[18] Dragomir-Daescu, D., Salas, C., Uthamaraj, S., and Rossman, T., 2015, "Quantitative Computed Tomography-Based Finite Element Analysis Predictions of Femoral Strength and Stiffness Depend on Computed Tomography Settings," J. Biomech., 48(1), pp. 153–161.

[19] Carbone, V., Fluit, R., Pellikaan, P., van der Krogt, M. M., Janssen, D., Damsgaard, M., Vigneron, L., Feilkas, T., Koopman, H. F., and Verdonschot, N., 2015, "TLEM 2.0—A Comprehensive Musculoskeletal Geometry Dataset for Subject-Specific Modeling of Lower Extremity," J. Biomech., 48(5), pp. 734–741.

[20] Klein Horsman, M. D., Koopman, H. F., van der Helm, F. C., Prose, L. P., and Veeger, H. E., 2007, "Morphological Muscle and Joint Parameters for Musculoskeletal Modelling of the Lower Extremity," Clin. Biomech., 22(2), pp. 239–247.

[21] Andersen, M. S., Damsgaard, M., MacWilliams, B., and Rasmussen, J., 2010, "A Computationally Efficient Optimisation-Based Method for Parameter Identification of Kinematically Determinate and Over-Determinate Biomechanical Systems," Comput. Methods Biomech. Biomed. Eng., 13(2), pp. 171–183.

[22] Taddei, F., Cristofolini, L., Martelli, S., Gill, H. S., and Viceconti, M., 2006, "Subject-Specific Finite Element Models of Long Bones: An In Vitro Evaluation of the Overall Accuracy," J. Biomech., 39(13), pp. 2457–2467.

[23] Fernandez, J. W., Mithraratne, P., Thrupp, S. F., Tawhai, M. H., and Hunter, P. J., 2004, "Anatomically Based Geometric Modelling of the Musculo-Skeletal System and Other Organs," Biomech. Model Mechanobiol., 2(3), pp. 139–155.

[24] Zhang, J., Sorby, H., Clement, J., Thomas, C. D. L., Hunter, P., Nielsen, P., Lloyd, D., Taylor, M., and Besier, T., 2014, "The MAP Client: User-Friendly Musculoskeletal Modelling Workflows," 6th International Symposium, ISBMS 2014, F. Bello and S. Cotin, eds. Strasbourg, France, pp. 182–192.

[25] Bradley, C. P., Pullan, A. J., and Hunter, P. J., 1997, "Geometric Modeling of the Human Torso Using Cubic Hermite Elements," Ann. Biomed. Eng., 25(1), pp. 96–111.

[26] Morgan, E. F., Bayraktar, H. H., and Keaveny, T. M., 2003, "Trabecular Bone Modulus-Density Relationships Depend on Anatomic Site," J. Biomech., 36(7), pp. 897–904.

[27] Sandino, C., McErlain, D. D., Schipilow, J., and Boyd, S. K., 2015, "The Poro-Viscoelastic Properties of Trabecular Bone: A Micro Computed Tomography-Based Finite Element Study," J. Mech. Behav. Biomed. Mater., **44**, pp. 1–9.

[28] Maxian, T. A., Brown, T. D., and Weinstein, S. L., 1995, "Chronic Stress Tolerance Levels for Human Articular Cartilage: Two Nonuniform Contact Models Applied to Long-Term Follow-Up of CDH," J. Biomech., **28**(2), pp. 159–166.

[29] Bergmann, G., Graichen, F., and Rohlmann, A., 1993, "Hip Joint Loading During Walking and Running, Measured in Two Patients," J. Biomech., **26**(8), pp. 969–990.

[30] Bergmann, G., Deuretzbacher, G., Heller, M., Graichen, F., Rohlmann, A., Strauss, J., and Duda, G. N., 2001, "Hip Contact Forces and Gait Patterns From Routine Activities," J. Biomech., **34**(7), pp. 859–871.

[31] Brand, R. A., Pedersen, D. R., Davy, D. T., Kotzar, G. M., Heiple, K. G., and Goldberg, V. M., 1994, "Comparison of Hip Force Calculations and Measurements in the Same Patient," J. Arthroplasty, **9**(1), pp. 45–51.

[32] D'Lima, D. D., Patil, S., Steklov, N., Slamin, J. E., and Colwell, C. W., Jr., 2005, "The Chitranjan Ranawat Award: In Vivo Knee Forces After Total Knee Arthroplasty," Clin. Orthop. Relat. Res., **440**, pp. 45–49.

[33] Taylor, S. J., Walker, P. S., Perry, J. S., Cannon, S. R., and Woledge, R., 1998, "The Forces in the Distal Femur and the Knee During Walking and Other Activities Measured by Telemetry," J. Arthroplasty, **13**(4), pp. 428–437.

[34] Taylor, S. J., and Walker, P. S., 2001, "Forces and Moments Telemetered From Two Distal Femoral Replacements During Various Activities," J. Biomech., **34**(7), pp. 839–848.

[35] Lu, T. W., Taylor, S. J., O'Connor, J. J., and Walker, P. S., 1997, "Influence of Muscle Activity on the Forces in the Femur: An In Vivo Study," J. Biomech., **30**(11–12), pp. 1101–1106.

[36] Hamner, S. R., Seth, A., and Delp, S. L., 2010, "Muscle Contributions to Propulsion and Support During Running," J. Biomech., **43**(14), pp. 2709–2716.

[37] Hillam, R. A., Goodship, A. E., and Skerry, T. M., 2015, "Peak Strain Magnitudes and Rates in the Tibia Exceed Greatly Those in the Skull: An In Vivo Study in a Human Subject," J. Biomech., **48**(12), pp. 3292–3298.

[38] Al Nazer, R., Lanovaz, J., Kawalilak, C., Johnston, J. D., and Kontulainen, S., 2012, "Direct In Vivo Strain Measurements in Human Bone: A Systematic Literature Review," J. Biomech., **45**(1), pp. 27–40.

[39] Detmer, D. E., Sharpe, K., Sufit, R. L., and Girdley, F. M., 1985, "Chronic Compartment Syndrome: Diagnosis, Management, and Outcomes," Am. J. Sports Med., **13**(3), pp. 162–170.

[40] Matheson, G. O., Clement, D. B., McKenzie, D. C., Taunton, J. E., Lloyd-Smith, D. R., and MacIntyre, J. G., 1987, "Stress Fractures in Athletes. A Study of 320 Cases," Am. J. Sports Med., **15**(1), pp. 46–58.

[41] Bennell, K. L., and Brukner, P. D., 1997, "Epidemiology and Site Specificity of Stress Fractures," Clin. Sports Med., **16**(2), pp. 179–196.

[42] Huang, T. W., and Kuo, A. D., 2014, "Mechanics and Energetics of Load Carriage During Human Walking," J. Exp. Biol., **217**(Pt. 4), pp. 605–613.

[43] Keller, T. S., Weisberger, A. M., Ray, J. L., Hasan, S. S., Shiavi, R. G., and Spengler, D. M., 1996, "Relationship Between Vertical Ground Reaction Force and Speed During Walking, Slow Jogging, and Running," Clin. Biomech., **11**(5), pp. 253–259.

[44] Komi, P. V., Fukashiro, S., and Jarvinen, M., 1992, "Biomechanical Loading of Achilles Tendon During Normal Locomotion," Clin. Sports Med., **11**(3), pp. 521–531.

[45] Yoshikawa, T., Mori, S., Santiesteban, A. J., Sun, T. C., Hafstad, E., Chen, J., and Burr, D. B., 1994, "The Effects of Muscle Fatigue on Bone Strain," J. Exp. Biol., **188**, pp. 217–233.

[46] Majewski, M., Susanne, H., and Klaus, S., 2006, "Epidemiology of Athletic Knee Injuries: A 10-Year Study," Knee, **13**(3), pp. 184–188.

[47] Burr, D. B., Forwood, M. R., Fyhrie, D. P., Martin, R. B., Schaffler, M. B., and Turner, C. H., 1997, "Bone Microdamage and Skeletal Fragility in Osteoporotic and Stress Fractures," J. Bone Miner. Res., **12**(1), pp. 6–15.

[48] Demers, M. S., Pal, S., and Delp, S. L., 2014, "Changes in Tibiofemoral Forces Due to Variations in Muscle Activity During Walking," J. Orthop. Res., **32**(6), pp. 769–776.

[49] Schneider, E., Michel, M. C., Genge, M., Zuber, K., Ganz, R., and Perren, S. M., 2001, "Loads Acting in an Intramedullary Nail During Fracture Healing in the Human Femur," J. Biomech., **34**(7), pp. 849–857.

[50] Cavanagh, P. R., and Komi, P. V., 1979, "Electromechanical Delay in Human Skeletal Muscle Under Concentric and Eccentric Contractions," Eur. J. Appl. Physiol. Occup. Physiol., **42**(3), pp. 159–163.

[51] Yang, N. H., Nayeb-Hashemi, H., Canavan, P. K., and Vaziri, A., 2010, "Effect of Frontal Plane Tibiofemoral Angle on the Stress and Strain at the Knee Cartilage During the Stance Phase of Gait," J. Orthop. Res., **28**(12), pp. 1539–1547.

[52] Lu, Y. C., and Untaroiu, C. D., 2013, "Statistical Shape Analysis of Clavicular Cortical Bone With Applications to the Development of Mean and Boundary Shape Models," Comput. Methods Prog. Biomed., **111**(3), pp. 613–628.